Computers and Concrete, *Vol. 20, No. 6 (2017) 635-643*
DOI: https://doi.org/10.12989/cac.2017.20.6.635

Effect of curing conditions on mode-II debonding between FRP and concrete: A prediction model

Pengcheng Jiao*[1], Sepehr Soleimani[2], Quan Xu[3], Lulu Cai**[4] and Yuanhong Wang[5]

[1]*Department of Civil and Environmental Engineering, Zhejiang University, Hangzhou 310000, Zhejiang, China*
[2]*Department of Civil and Environmental Engineering, Michigan State University, East Lansing, MI 48824, USA*
[3]*State Key Laboratory of Heavy Oil Processing, China University of Petroleum (Beijing), Beijing 102249, China*
[4]*Personalized Drug Therapy Key Laboratory of Sichuan Province, Hospital of the University of Electronic Science and Technology of China and Sichuan Provincial People's Hospital, Chengdu 610072, China*
[5]*Center of Analysis and Testing, Institute of Analytical Chemistry for Life Science, School of Public Health, Nantong University, Nantong 226019, China*

(Received December 9, 2016, Revised July 9, 2017, Accepted July 10, 2017)

Abstract. The rehabilitation and strengthening of concrete structures using Fiber-Reinforced Polymer (FRP) materials have been widely investigated. As a priority issue, however, the effect of curing conditions on the bonding behavior between FRP and concrete structures is still elusive. This study aims at developing a prediction model to accurately capture the mode-II interfacial debonding between FRP strips and concrete under different curing conditions. Single shear debonding experiments were conducted on FRP-concrete samples with respect to different curing time *t* and temperatures *T*. The *J*-integral formulation and constrained least square minimization are carried out to calibrate the parameters, i.e., the maximum slip $\bar{s}$ and stretch factor n. The prediction model is developed based on the cohesive model and Arrhenius relationship. The experimental data are then analyzed using the proposed model to predict the debonding between FRP and concrete, i.e., the interfacial shear stress-slip relationship. A Finite Element (FE) model is developed to validate the theoretical predictions. Satisfactory agreements are obtained. The prediction model can be used to accurately capture the bonding performance of FRP-concrete structures.

Keywords: FRP-concrete; mode-II debonding; prediction model; cohesive model; Arrhenius relationship

1. Introduction

Thanks to the advantages of high strength- and stiffness-to-weight ratios and well environmental durability, composite materials have been widely used in structural repair and strengthening for decades (Buyukozturk *et al.* 2004). However, debonding between externally bonded composites and concrete structures critically impacts the stability of laminate-strengthened civil infrastructures. In order to sufficiently prevent debonding-induced damages from happening in civil infrastructures, various techniques have been developed, e.g., postbuckling-based damage detection mechanism, wireless sensors for structural health monitoring, etc. (Lajnef *et al*. 2013, Alavi *et al.* 2016, 2017, Jiao *et al*. 2016, 2017a, b, c, Hasni *et al*. 2017a, b, Soleimani *et al.* 2017). Fiber-Reinforced Polymer (FRP) is one of the extensively applied composite materials in strengthening and retrofitting concrete structures, given the advantages, e.g., light weight, high installation flexibility, well strength and ductility contributions, and well corrosion resistance (Teng *et al.* 2006, Freddi and Savoia 2008, Mazzotti *et al*. 2009). However, interfacial debonding is commonly reported in FRP-strengthening technique. Many studies have been carried out to predict the bonding mechanism of FRP-concrete structures. Since the interfacial debonding is significantly affected by curing conditions, research effort has been particularly dedicated to investigating the effect of different conditions, namely moisture conditioning, temperature, fire, and freeze and thaw cycles (Benzarti *et al.* 2011, Kodur and Yu 2016).

In order to capture the structural response of FRP-concrete and predict the interfacial debonding under different conditions, many prediction models have been proposed (Yuan *et al.* 2004, Ferracuti *et al.* 2007). Choi and Cheung (1996) presented a tension stiffening model to predict the final cracking point and steel yielding in steel-reinforced concrete members. Wu *et al.* (2002) studied the mode and mechanism of debonding failure under different conditions, e.g., moisture, temperature, freeze and thaw cycles, etc., to predict the long-term durability of FRP-strengthened concrete structures. The authors presented a long-term model to predict the mode-II debonding between externally-bonded FRP and concrete with respect to interfacial *ERR*, using short-term data from accelerated aging experiments. Ouyang and Wan (2009) investigated debonding failures of FRP-concrete members using an energy approach. The authors employed the compliance method and *J*-integral to demonstrate the extension behavior of interfacial crack. Tuakta and Buyukozturk

∗Corresponding author, Ph.D.
E-mail: pjiao@zju.edu.cn
∗∗Ph.D.
E-mail: cailulu@med.uestc.edu.cn

ISSN: 1598-8198 (Print), 1598-818X (Online)

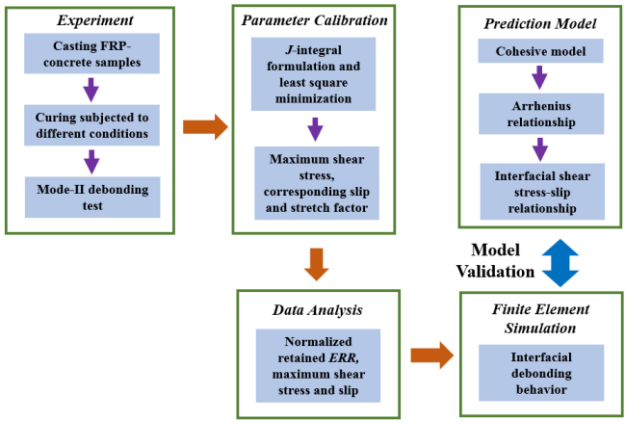

Fig. 1 Flow chart illustrating the work conducted in this study

(2011) concluded that the failure type of carbon FRP (CFRP)-strengthened concrete samples subjected to different curing conditions could be changed from concrete failure to cohesive layer failure, which was mainly due to the sharp mechanical property degradation the bonding agent. However, this significant decreasing was not reflected in the ultimate shear load by having a redistribution of the load transfer zone along the interface. Such redistribution was also discussed in Benzarti *et al.* (2011). The compliance methods have been carried out based on the changes of potential ERR due to crack extension Xiao *et al.* (2012). Foraboschi (2012) developed a prediction model to measure the delayed debonding and lifetime of concrete members with externally bonded FRP. The author considered the effect of crack growth rate in the mesoscale with respect to interfacial bond shear stress and crack length. Barbieri *et al.* (2016) experimentally examined the scaling phenomena in FRP-concrete members with respect to different bonding lengths and widths. The experimental results were compared with numerical simulations based on nonlinear constitutive model. However, lack of sufficient prediction models has been developed to predict the potential debonding failure of FRP-concrete structures subjected to different curing conditions This study aims at developing a prediction model to investigate the effect of curing conditions on mode-II debonding between externally bonded FRP strips and concrete structures. In order to achieve the research objective, this work can be deployed as follows,

• Section 2 presents the experiments of FRP-concrete samples subjected to different curing time t and temperatures T. The experimental results are provided in terms of maximum axial force N.

• Section 3 proposes parameter calibrations of maximum shear stress, corresponding slip and stretch factor. A prediction model is then developed using the cohesive model and Arrhenius relationship.

• Section 4 studies the experimental data using the proposed model. In particular, the normalized percentages of retained *ERR*, maximum shear stress and slip are obtained.

• Section 5 introduces a Finite Element (FE) model to numerically validate the theoretical predictions, i.e., interfacial shear stress-slip relationship, obtained from the proposed model. Satisfactory agreements are obtained from the comparisons between the theoretical and numerical results to demonstrate the accuracy of the prediction model. Fig. 1 presents a flow chart to illustrate the work conducted in this study.

Table 1 Mix proportions of the concrete samples and material properties of the FRP strips

Concrete				FRP Strips	
Mix Proportions (Weight ratios to the Portland cement)			Air Admixture (mL/m^3)		
Coarse Aggregate	Fine Aggregate	Water		Tensile Strength (MPa)	Young's Modulus (GPa)
2.5	1.82	0.5	1047.73	3000	230

Table 2 Ions in the exposure deionized water

	Ion							
	Al	Ca	Fe	Mg	Mn	Na	K	Cl
Quantity ($\frac{mg}{L}$)	< 0.1	0.5	1.32	1.8	< 0.1	5	< 0.1	0.1

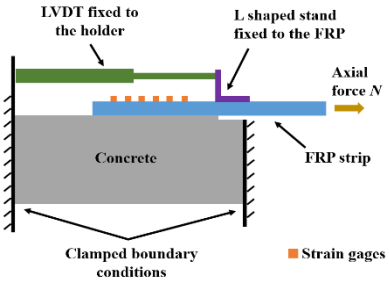

(a) Graphical illustration of the testing setup

(b) Single shear debonding test using MTS loading machine

Fig. 2 Experimental setup of the single shear test

2. Experiments

2.1 Materials, curing conditions and testing procedures

Normal concrete samples were casted in this study using Portland cement. The geometry properties of the concrete and FRP strips were: 330×127×102 mm^3 and 160×46×1.65 mm^3, respectively. The concrete specimens were cured in lime saturated water for 28 days, and then dried in room temperature for 72 days. After sanded the surfaces of the samples, epoxy was used as the bonding agent to bond between the FRP strips and concrete using a dry-layup

Table 3 Maximum axial force obtained from the experiments with respect to curing time and temperature

Group	Case	Curing Time t (weeks)	Temperature T (°C)	Maximum Axial Force N (kN)
I	T_1W_3	3	25	11.143
	T_1W_5	5		12.048
	T_1W_7	7		12.314
	T_1W_9	9		11.896
	T_1W_{11}	11		11.930
	T_1W_{13}	13		10.988
II	T_2W_3	3	36	12.796
	T_2W_5	5		12.592
	T_2W_7	7		11.870
	T_2W_9	9		11.074
	T_2W_{11}	11		11.149
	T_2W_{13}	13		10.660
III	T_3W_3	3	48	11.906
	T_3W_5	5		11.966
	T_3W_7	7		11.158
	T_3W_9	9		10.588
	T_3W_{11}	11		10.707
	T_3W_{13}	13		9.429
IV	T_4W_3	3	60	12.578
	T_4W_5	5		10.734
	T_4W_7	7		11.098
	T_4W_9	9		8.928
	T_4W_{11}	11		7.891
	T_4W_{13}	13		9.150

technique. The FRP-concrete specimens were cured in room temperature for 7 days, and then placed in temperature-adjusted deionized water until they were tested. The curing temperatures of the deionized water were controlled as: $T_1 = 25℃$, $T_2 = 36\,℃$, $T_3 = 48\,℃$, and $T_4 = 60\,℃$ for 3, 5, 7, 9, 11, and 13 weeks, respectively. Table 1 summarizes the mix proportions of the concrete samples and material properties of the FRP strips. In particular, the coarse and fine aggregates and water are given by the mix proportions defined as the weight ratios to Portland cement. Table 2 displays the ion quantities of the deionized water used in the experiments. Fig. 2 shows the experimental setup of the single shear (mode-II) tests conducted in this study. Fig. 2(a) graphically illustrates the testing setup, and Fig. 2(b) indicates the debonding experiments carried out by using a MTS loading machine. In order to capture the interfacial debonding between the FRP strips and concrete samples, 6 strain gages were attached to the strain region of the FRP surface for each tested sample. Linear Variable Displacement Transformer (LVDT) was deployed to measure the relative displacement at crack tips.

2.2 Experimental results

Table 3 summarizes the maximum axial force N obtained from the experiments with respect to curing period t and temperature T. Each case consists of three testing samples and the maximum axial force is obtained as the average of the three experimental results. It can be seen that the axial force is qualitatively reduced when the curing time in deionized water is increased. However, the curing temperature is not as critical to the loading capacity as the curing time and, therefore, the axial forces obtained from different testing groups are relatively comparable.

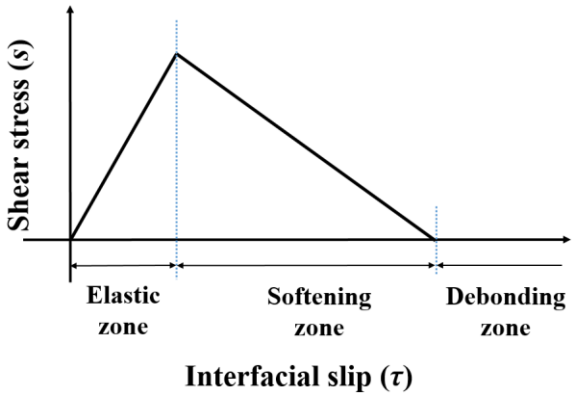

Fig. 3 Bilinear cohesive zone model

3. Parameter calibrations and prediction model

3.1 Parameter calibrations of maximum shear stress $\bar{\tau}$, corresponding slip $\bar{s}$, and stretch factor n

This section presents a prediction model on the mode-II debonding between externally bonded FRP and concrete subjected to different curing conditions. In order to develop the model, it is of necessity to introduce certain assumptions. In particular, the following simplifications are drawn in this study,

- FRP strips are uniformly bonded to concrete such that the entire bonding interfaces have the same material and mechanical properties;
- Interfacial dobonding occurs when *ERR* reaches the critical value of crack-tip *ERR*, i.e., $J = J_{tip}$;
- Bilinear cohesive zone model is used as the material law to define the bonding interface between FRP and concrete, as shown in Fig. 3;
- Single-dominant degradation mechanism is not changed with respect to the variations of time or temperature during exposure. However, the degradation rate is accelerated with the increasing of temperature; and
- Crack gradually extends until FRP strips are completely debonded from concrete.

The *J*-integral is used to formulate the *ERR* at crack tip. Selecting a closed path surrounding the crack tip as the integration path, the *J*-integral is given as (Rice 1988),

$$J = \oint_C \left(V_o \mathrm{d}z + u_{i,1}\sigma_{ij}n_j \mathrm{d}x\right) \tag{1}$$

The *J*-integral in Eq. (1) might be rewritten as (Wang and Qiao 2004),

$$J = \frac{1}{2}\left(C_N N^2 + C_Q Q^2 + C_M M^2 + C_{MN} MN + C_{NQ} NQ + C_{MQ} MQ\right) \quad (2)$$

where *N*, *Q* and *M* are the axial force, transverse shear force and bending moment, respectively. The corresponding stiffness coefficients are,

$$\begin{cases} C_N = \dfrac{1}{C_{FRP}} + \dfrac{1}{C_C} + \dfrac{(h_{FRP} + h_C)^2}{4D_C} \\ C_Q = \dfrac{1}{B_{FRP}} + \dfrac{1}{B_C} \\ C_M = \dfrac{1}{D_{FRP}} + \dfrac{1}{D_C} \\ C_{MN} = \dfrac{h_{FRP} + h_C}{D_C} \\ C_{NQ} = k\left(\dfrac{1}{B_{FRP}} + \dfrac{1}{B_C}\right) h_{FRP} \\ C_{MQ} = 2k\left(\dfrac{1}{B_{FRP}} + \dfrac{1}{B_C}\right) \end{cases} \quad (3)$$

where the subscripts *FRP* and *C* represent the FRP strip and concrete, respectively. *h*, *k*, *C*, *B* and *D* refer to the layer thickness, decay rater determined by the geometry and material properties of the specimen, axial, shear and bending stiffness coefficients, respectively.

Substituting Eq. (3) into Eq. (2), the *J*-integral can be reduced to,

$$J = \frac{N^2}{2\, {b_{FRP}}^2\, h_{FRP}\, E_{FRP}} + \frac{Q^2}{2k}\left(\frac{1}{G_{FRP} h_{FRP}} + \frac{1}{G_C h_C}\right) \quad (4)$$

where b_{FRP}, h_{FRP}, E_{FRP}, G_{FRP}, h_C and G_C are the width, thickness, longitudinal and transverse shear modulus of the FRP, and the thickness and transverse shear modulus of the concrete, respectively. Since only single shear debonding, i.e., mode-II debonding, is taken into account in this study, the axial force *N* is dominant in Eq. (4), while the shear force *Q* may be negligible. Therefore, Eq. (4) is reduced to,

$$J = \alpha N^2 \quad (5)$$

where $\alpha = \frac{1}{2\, {b_{FRP}}^2\, h_{FRP}\, E_{FRP}}$.

According to the fractional law proposed in Mazzotti *et al.* (2009), the distribution of interfacial shear stress τ can be written in terms of the slide between FRP and concrete *s* as,

$$\tau = \frac{\bar{\tau} s}{\bar{s}} \frac{n}{n - 1 + (\frac{s}{\bar{s}})^n} \quad (6)$$

where $\bar{\tau}$, $\bar{s}$ and *n* denote the maximum shear stress, maximum slip, and stretch factor that governs the softening branch ($n > 2$), respectively.

Based on the traction-separation model, the fracture energy is given with respect to the maximum shear stress and corresponding slip as (Ferracuti *et al*. 2007, Mazzotti *et al*. 2009),

$$J = \int_0^\infty \tau ds = g_f\, \bar{\tau}\, \bar{s} \quad (7)$$

where g_f is defined with respect to the stretch factor *n* as,

$$g_f = \pi \left(\frac{1}{n-1}\right)^{1-\frac{2}{n}} \sin\left(\frac{2\pi}{n}\right)^{-1} \quad (8)$$

Substituting Eq. (7) into Eq. (5), we obtain,

$$\bar{\tau} = \frac{\alpha N^2}{g_f\, \bar{s}} \quad (9)$$

Taking Eq. (9) into Eq. (6), the interfacial shear stress distribution yields,

$$\tau = \frac{\alpha s N^2}{g_f\, \bar{s}^2} \cdot \frac{n}{n - 1 + \left(\frac{s}{\bar{s}}\right)^n} \quad (10)$$

In order to determine the shear stress-slip relationship in Eq. (10), two unknown parameters, i.e., $\bar{s}$ and *n*, need to be solved. The factors can be determined using a constrained, two-parameter least square minimization (Ferracuti *et al*. 2007),

$$\min_{\bar{s},n} \left[\sum_{i=1}^{m} \left[\tau_i(\bar{s}, n) - \tau_{exp,i}\right]^2\right] \quad (11a)$$

with respective to the constraint defined by Eqs. (5) and (7) as,

$$J = g_f(n)\, \bar{\tau}\, \bar{s} = \frac{{N_{\mathrm{Max},exp}}^2}{2\, {b_{FRP}}^2\, h_{FRP}\, E_{FRP}} \quad (11b)$$

where *i*, *m* and $N_{\mathrm{Max},exp}$ are the summation index, stopping point upper limit of the summation, and maximum transmittable force obtained from the experiment, respectively.

In order to carry out the minimization in Eq. (11), the experimental data of the shear stress and corresponding slip, i.e., $\tau_{i+\frac{1}{2}}$ and $s_{i+\frac{1}{2}}$, and fracture energy J are used. In particular, the average shear stress between two subsequent strain gauges $\tau_{i+\frac{1}{2}}$ is calculated as a function of the distance of measured strains ε_i and ε_{i+1} as,

$$\tau_{i+\frac{1}{2}} = -\frac{E_{FRP} A_{FRP} (\varepsilon_{i+1} - \varepsilon_i)}{b_{FRP} (x_{i+1} - x_i)} \quad (12)$$

where A_{FRP} and *x* refer to the area of the FRP strip and measured location in the longitudinal direction, respectively. The average slip $s_{i+\frac{1}{2}}$ is measured as,

$$s_{i+\frac{1}{2}} = \frac{1}{2}[s(x_{i+1}) + s(x_i)] \quad (13)$$

where *s* is given as a function of *x*,

$$s(x) = s(x_{i+1}) - \frac{1}{2}\frac{\varepsilon_{i+1} - \varepsilon_i}{x_{i+1} - x_i}(x_{i+1} - x)^2 + \varepsilon_i (x_{i+1} - x) \quad (14)$$

The relationship between the maximum applied load and fracture energy J is given as (Ferracuti *et al*. 2007),

$$N_{max} = b_{FRP} \sqrt{2\, J E_{FRP} h_{FRP}} \quad (15)$$

Therefore, the unknown parameters, i.e., $\bar{s}$ and n, can be numerically determined using the minimization. Substituting the solved factors into Eq. (10), interfacial shear stress distribution can be obtained.

3.2 Prediction model

The Arrhenius relationship is used to define the normalized percentage of retained *ERR* (J_{norm}). Note that the normalization in this study is obtained with respect to the control conditions, i.e., curing time is 13 weeks and temperature is 60°C (T_4W_{13} in Table 3). The normalized percentage of retained *ERR* is,

$$J_{norm} = 100\frac{J}{J_0} = (100 - \beta_J)\,\mathrm{e}^{\left[A_J t\,\mathrm{e}^{\left(-\frac{B_J}{T}\right)}\right]} + \beta_J \tag{16}$$

where J_0, β_J, A_J and B_J refer to the *ERR* under the control conditions, percentages of the retained *ERR*, and two Arrhenius coefficients, respectively. Due to the mechanical interlocking left in the interface, β_J is assumed to be independent of curing temperature. Note that $B_J = \frac{E_a}{R}$, where E_a and R are the activation energy and gas constant, respectively.

In the same manner, the normalized percentages of maximum shear stress $\bar{\tau}_{norm}$ and corresponding slip $\bar{s}_{norm}$ can be obtained. Therefore, we obtain the normalized percentages as,

$$\begin{aligned}(J_{norm}, \bar{\tau}_{norm}, \bar{s}_{norm}) &= 100\left(\frac{J}{J_0}, \frac{\bar{\tau}}{\bar{\tau}_0}, \frac{\bar{s}}{\bar{s}_0}\right) \\ &= (100 - \beta_{J,\bar{\tau},\bar{s}})\,\mathrm{e}^{\left[-A_{J,\bar{\tau},\bar{s}}\,t\mathrm{e}^{\left(-\frac{B_{J,\bar{\tau},\bar{s}}}{T}\right)}\right]} \\ &\quad + \beta_{J,\bar{\tau},\bar{s}}\end{aligned} \tag{17}$$

where $\bar{\tau}_0$ and $\bar{s}_0$ refer to the maximum shear stress and slip under the control conditions. Substituting Eq. (17) into Eq. (10), the shear stress distribution with respective to curing time t and temperature T is obtained as

$$\tau = \frac{\Phi_{\bar{\tau}}}{\Phi_{\bar{s}}} \cdot \frac{\bar{\tau}s}{\bar{s}_0} \frac{n}{n - 1 + \left(\frac{100s}{\Phi_{\bar{s}}}\right)^n} \tag{18}$$

where $\bar{\tau}$ is given by Eq. (9) and

$$\begin{cases} \Phi_{\bar{\tau}} = (100 - \beta_{\bar{\tau}})\mathrm{e}^{\left[-A_{\bar{\tau}}\,t\,\mathrm{e}^{\left(-\frac{B_{\bar{\tau}}}{T}\right)} + \beta_{\bar{\tau}}\right]} \\ \Phi_{\bar{s}} = (100 - \beta_{\bar{s}})\mathrm{e}^{\left[-A_{\bar{s}}\,t\,\mathrm{e}^{\left(-\frac{B_{\bar{s}}}{T}\right)} + \beta_{\bar{s}}\right]} \end{cases} \tag{19}$$

4. Experimental results analysis

The prediction model developed in Section 3.2 is used to analyze the experimental results. In particular, Eq. (17) is applied to obtain the normalized percentages of retained *ERR*, maximum shear stress and slip based on the testing data. Table 4 summarizes the coefficients, i.e., *A*, *B*, and *β*, gained from the experiments.

Table 4 Coefficients for normalized percentage of retained *ERR*, maximum shear stress and corresponding slip

	A		*B*		*β*
A_J	3.635×10^5	B_J	5644	β_J	24.54
$A_{\bar{\tau}}$	7.26×10^5	$B_{\bar{\tau}}$	5863	$\beta_{\bar{\tau}}$	63.66
$A_{\bar{s}}$	1.118×10^6	$B_{\bar{s}}$	5984	$\beta_{\bar{s}}$	60.21

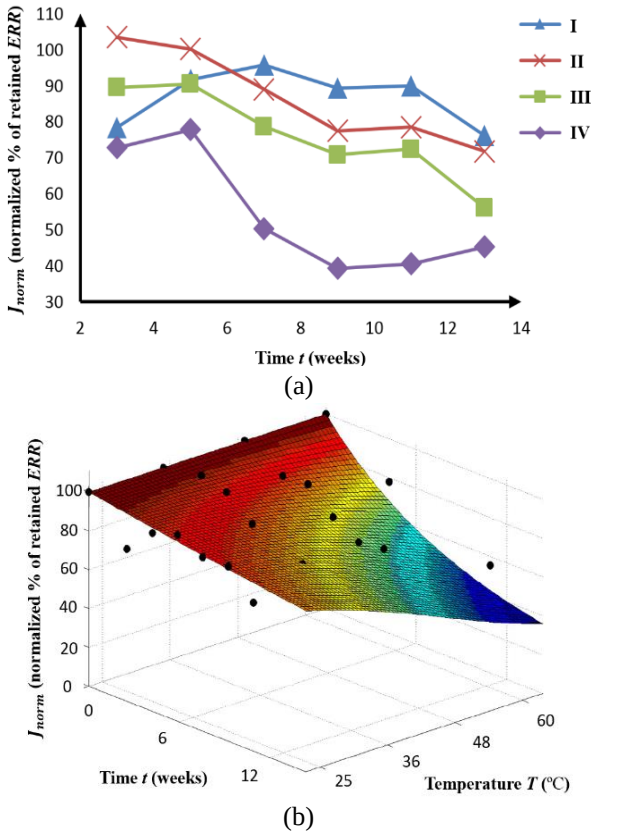

Fig. 4(a) Normalized percentage of retained *ERR* *vs.* curing time under different temperatures, and (b) corresponding fitting surface

4.1 Normalized percentage of retained ERR (J_{norm})

Fig. 4 displays the relationships between the retained *ERR* and curing time with respect to the four temperatures, i.e., Group I (T_1 = 25 °C), Group II (T_2 = 36 °C), Group III (T_3 = 48 °C), and Group IV (T_4 = 60 °C). Fig. 4(a) shows that J_{norm} is increased within the first 7 and 5 weeks for Group I and Group IV, respectively. A slight increasing is observed from Group IV from week 9 to week 13. In other cases, both the curing time and temperature negatively affect the percentage of retained *ERR*. Fig. 4(b) presents the corresponding fitting surface of J_{norm} with respect to the curing time and temperature. It can be seen that the distributed trend is inversely proportional to both time and temperature. In addition, the retained *ERR* is impacted more significantly when the curing time is longer than 11 weeks

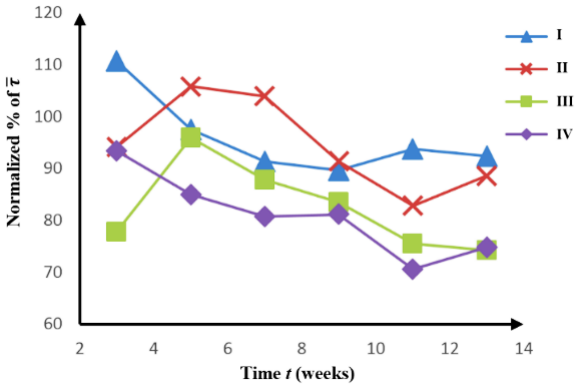

(a)

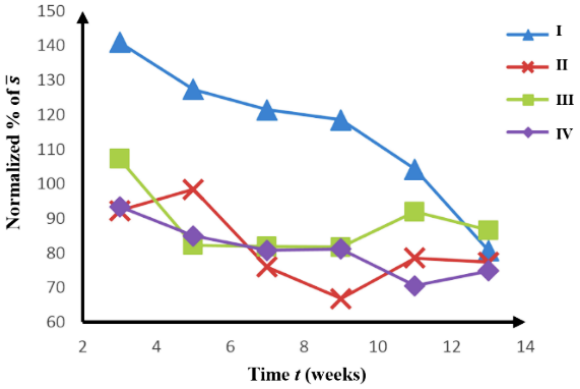

(b)

Fig. 5 Normalized percentages of (a) maximum shear stress $\overline{\tau}$ and (b) corresponding slip $\overline{s}$ with respect to time and temperature

and the temperature is higher than 60°C.

4.2 Normalized percentages of maximum shear stress $\overline{\tau}_{norm}$ and Slip $\overline{s}_{norm}$

Fig. 5 presents the effect of curing time and temperature on the normalized percentages of maximum shear stress $\overline{\tau}_{norm}$ and corresponding slip $\overline{s}_{norm}$.

It can be seen in Fig. 5(a) that $\overline{\tau}_{norm}$ is significantly affected by conditioning time. Groups I and IV have the same variation pattern while Groups II and III are similar. In Fig. 5(b), Groups II, III and IV perform relatively low sensitivity to curing time. However, a critical effect of curing time is found on Group I. More detailed values of the normalized percentages of maximum shear stress and corresponding slip are presented in Table 5.

5. Numerical validation

5.1 FE model

Numerical simulations were carried out in this section to validate the prediction model. The FE model was developed using ABAQUS v6.12. The FRP was simulated as a solid composite layer and the concrete was defined as solid, homogenous. Clamped boundary conditions were applied to the ends of the concrete sample and a single axial force N was placed on the FRP strip, as shown in Fig. 6. Table 6 summarizes the geometry and material properties, as well as the mesh information of the FRP-concrete model. A finer mesh, i.e., $\frac{1}{10}$ of the element size of the concrete, was proposed to the FRP strip.

The brittle cracking model was applied to simulate the mechanical response of the concrete, as the overall material

Table 5 Normalized percentages of maximum shear stress and corresponding slip

Group	Case	Curing Time (weeks)	Temp. (°C)	$\overline{\tau}$ (MPa)	Normalized (%) of $\overline{\tau}$	$\overline{s}$×1000 (10^{-4} mm)	Normalized (%) of $\overline{s}$
I	T_1W_3	3	25	5.39	110.83	799.08	140.95
	T_1W_5	5		4.98	97.54	747.31	127.37
	T_1W_7	7		4.60	91.35	687.46	121.42
	T_1W_9	9		4.36	89.64	672.08	118.55
	T_1W_{11}	11		4.56	93.77	591.06	104.26
	T_1W_{13}	13		4.48	92.44	463.04	80.68
II	T_2W_3	3	36	4.58	94.18	523.24	92.27
	T_2W_5	5		5.14	105.82	571.58	98.46
	T_2W_7	7		5.05	103.99	430.53	75.94
	T_2W_9	9		4.44	91.41	378.71	66.80
	T_2W_{11}	11		4.03	82.87	445.52	78.58
	T_2W_{13}	13		4.29	88.61	438.40	77.33
III	T_3W_3	3	48	3.78	77.77	608.08	107.26
	T_3W_5	5		4.66	95.94	466.60	82.30
	T_3W_7	7		4.22	87.84	468.38	81.91
	T_3W_9	9		4.06	83.51	463.14	81.69
	T_3W_{11}	11		3.67	75.57	521.46	91.98
	T_3W_{13}	13		3.61	74.28	490.98	86.60
IV	T_4W_3	3	60	4.54	82.52	505.46	93.40
	T_4W_5	5		4.13	87.33	474.47	84.96
	T_4W_7	7		3.92	79.26	426.97	80.72
	T_4W_9	9		3.94	83.01	406.65	81.17
	T_4W_{11}	11		3.43	71.18	348.49	70.56
	T_4W_{13}	13		3.64	76.27	416.31	74.87

Table 6 Geometry and material properties of the FRP-concrete model

	FRP Strip		Concrete	
Geometry and Material Properties	Thickness (mm)	0.5	Height (mm)	100
	Width (mm)	45	Width (mm)	125
	Bonding Length (mm)	200	Length (mm)	330
	Young's Modulus (MPa)	10000, 74000, 10000	Young's Modulus (MPa)	26200
	Poisson's Ratio	0.3, 0.3, 0.3	Poisson's Ratio	0.12
	Shear Modulus (MPa)	5000, 5000, 4000	Shear Modulus (MPa)	--
Mesh Information	Element Number	1500	Element Number	10696
	Element Size	2	Element Size	20
	Element Type	Linear hexahedral C3D8R	Element Type	Solid C3D8R
	Material Type	Elastic, composite	Material Type	Elastic, homogenous

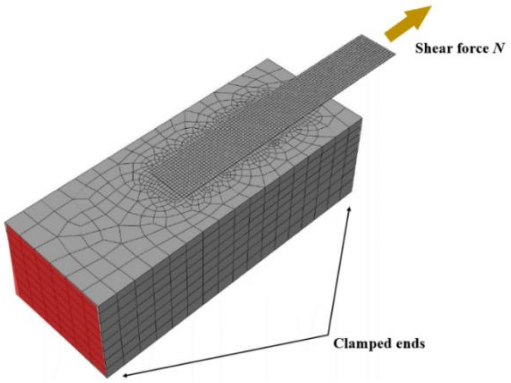

Fig. 6 Mesh of crack simulation between FRP strip and concrete

behavior was dominated by tensile cracking in this study. The interacting surface of the FRP and concrete was initially bonded using the surface-to-surface contact technique subjected to small sliding. Crack propagation was introduced by contour integrals. The contact before debonding was defined by the property option of cohesive behavior, and the contact after debonding was damage contact. The initial normal and shear stiffness properties, K_{nn} and K_{ss}, were assumed to be smaller than tensile stiffness, K_{tt}. The relationship of the stiffness coefficients were given as,

$$\mathbf{t} = \begin{bmatrix} t_n \\ t_s \\ t_t \end{bmatrix} = \begin{bmatrix} K_{nn} & K_{ns} & K_{nt} \\ K_{ns} & K_{ss} & K_{st} \\ K_{nt} & K_{st} & K_{tt} \end{bmatrix} \begin{bmatrix} \delta_n \\ \delta_s \\ \delta_t \end{bmatrix} = \mathbf{K\delta} \tag{20}$$

where K_{ns}, K_{nt}, and K_{st} were negligible.

The maximum stress criterion was used to simulate the changes of nominal stiffness due to the initiation of debonding damage, and the maximum stresses in the other two directions were given significantly larger than the crack extension. The cohesive model defined in Eq. (10) under different curing time and temperature was converted into a tabular damage variable, *D*, as

$$D = 1 - \frac{t_t}{T_t} \tag{21}$$

where t_t and T_t are the predicted stresses with and without damage initiation, respectively.

The debonding process of the FRP-concrete model is presented in Fig. 7. It can be seen that the FE model sufficiently predicts the debonding during crack extension, including (a) completely bonding, (b) initial debonding, (c) debonding extension, and (d) completely debonding. In order to better demonstrate the interfacial debonding between the FRP and concrete, a deformation scale factor of 10 is used to present the numerical results in the FE model and, therefore, the formed FRP strip in Fig. 7(b) seems to be disappeared under the concrete.

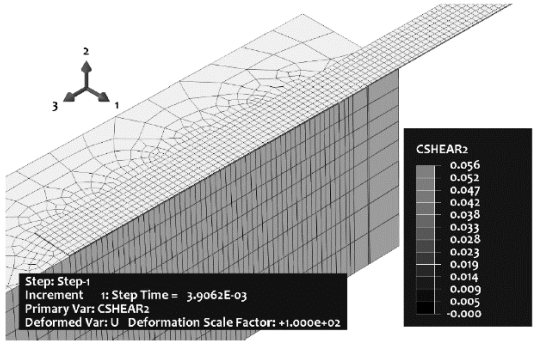

(a)

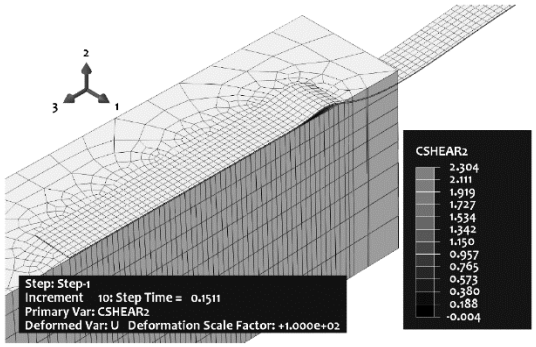

(b)

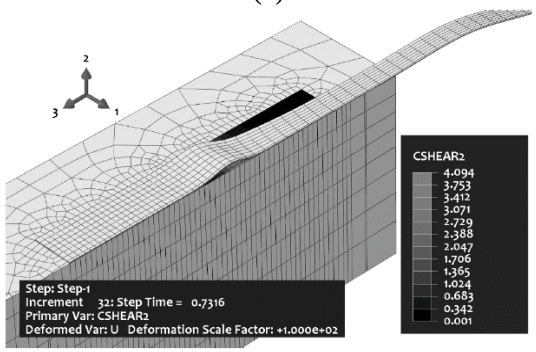

(c)

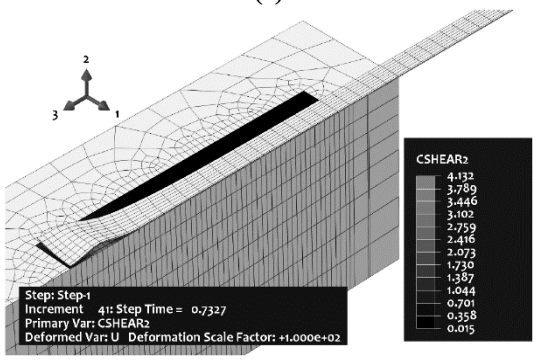

(d)

Fig. 7 Spectrums of interfacial crack extension: (a) completely bonding, (b) initial debonding, (c) debonding extension, and (d) completely debonding

5.2 Validation of the prediction model

The interfacial shear stress-slip relationship is compared between the FE results and theoretical predictions to validate the presented model, as shown in Fig. 8. The calibrated parameters based on the experimental results are used to obtain the shear stress distribution defined in Eq. (18). Satisfactory agreements are obtained between the predicated and experimental results. The presented model sufficiently predicts the debonding between FRP strips and concrete structures.

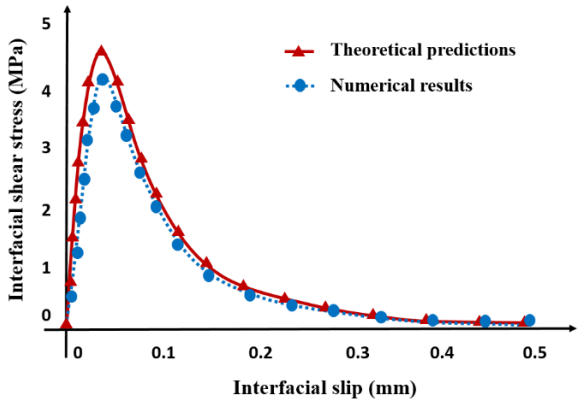

Fig. 8 Comparison of interfacial shear stress and slip between experimental results and numerical predictions that are based on the proposed assumptions

6. Conclusions

In this study, a prediction model was developed to investigate the effect of curing conditions on mode-II debonding between externally bonded FRP and concrete structures. Experiments were conducted on FRP-concrete samples subjected to different curing time t and temperatures T. The retained *ERR* was calibrated using the *J*-integral formulation and the maximum shear stress and corresponding slip were determined by the least square minimization. A prediction model was developed using the cohesive model and Arrhenius relationship. The experimental results were then analyzed using the proposed model. In particular, the parameters in the prediction model, i.e., normalized percentages of *ERR* J_{norm}, shear stress $\overline{\tau}_{norm}$ and corresponding slip $\overline{s}_{norm}$, were investigated. A FE model was developed to validate the theoretical predictions with respect to interfacial shear stress-slip relationship. Satisfactory agreements were observed between the theoretical and numerical results, which indicate the accuracy of the proposed model. The prediction model can be used as a design criterion to capture mode-II debonding of FRP-strengthened concrete structures.

Acknowledgments

The research presented in this paper was carried out through funding from the National Nature Science Foundation of China No. 51505501. All of the financial supports are gratefully acknowledged. The experiments of this work were partially conducted by Ms. F.S. Imani. The FE model was initially developed by Mr. M. Zahabi. The authors are grateful to their inspirational help.

References

Soleimani, S., Rajaei, S., Jiao, P. and Soheilinia, S. (2017), "New prediction models for unconfined compressive strength of geopolymer stabilized solid using multi-gen genetic programming", *Measure.*, **113**, 99-107.

Alavi, A.H., Hasni, H., Jiao, P., Borchani, W. and Chatti, K. (2017), "Fatigue cracking detection in steel bridge girders through a self-powered sensing concept", *J. Constr. Steel Res.*, **128**, 19-38.

Barbieri, G., Biolzi, L., Bocciarelli, M. and Cattaneo, S. (2016), "Size and shape effect in the pull-out of FRP reinforcement from concrete", *Compos. Struct.*, **143**, 395-417.

Benzarti, K., Chataigner, S., Quiertant, M., Marty, C. and Aubagnac, C. (2011), "Accelerate ageing behavior of the adhesive bond between concrete specimens and CFRP overlays", *Constr. Build. Mater.*, **25**(2), 523-538.

Buyukozturk, O., Gunes, O. and Karaca, E. (2004), "Progress on understanding debonding problems in reinforced concrete and steel members strengthened using FRP composites", *Constr. Build. Mater.*, **18**, 9-19.

Choi, C.K. and Cheung, S.H. (1996), "Tension stiffening model for planar reinforced concrete members", *Comput. Struct.*, **59**(1), 179-190.

Ferracuti, B., Savoia, M. and Mozzatti, C. (2007), "Interface law for FRP-concrete delamination", *Compos. Struct.*, **80**, 523-531.

Foraboschi, P. (2012), "Predictive multiscale model of delayed debonding for concrete members with adhesively bonded external reinforcement", *Compos.: Mech. Comput. Appl.*, **3**(4), 307-329.

Freddi, F. and Savoia, M. (2008), "Analysis of FRP-concrete debonding via boundary integral equations", *Eng. Fract. Mech.*, **75**(6), 1666-1683.

Hasni, H., Alavi, A.H., Jiao, P. and Lajnef, N. (2017), "Detection of fatigue cracking in steel bridge girders: A support vector machine approach", *Arch. Civil Mech. Eng.*, **17**, 609-622.

Hasni, H., Alavi, A.H., Jiao, P., Lajnef, N., Chatti, K., Aono, K. and Chakrabartty, S. (2017), "A new approach for damage detection in asphalt concrete pavements using battery-free wireless sensors with non-constant injection rates", *Measure.*, **110**, 217-229.

Jiao, P, Borchani, W., Alavi, A.H., Hasni, H. and Lajnef, N. (2017), "An energy harvesting and damage sensing solution based on post-buckling response of non-uniform cross-section beams", *Struct. Contr. Health Monitor.*, **e2052**, 1-19.

Jiao, P., Borchani, W., Hasni, H., Alavi, A.H. and Lajnef, N. (2016), "Post-buckling response of non-uniform cross-section bilaterally constrained beams", *Mech. Res. Commun.*, **78**, 42-50.

Jiao, P., Borchani, W., Hasni, H. and Lajnef, N. (2017), "A new solution of measuring thermal response of prestressed concrete bridge girders for structural health monitoring", *Measure. Sci. Technol.*, **28**(8), 085005.

Jiao, P., Borchani, W., Hasni, H. and Lajnef, N. (2017), "Static and dynamic post-buckling analyses of irregularly constrained beams under the small and large deformation assumptions", *J. Mech. Sci.*, **124**, 203-215.

Kodur, V.K.R. and Yu, B. (2016), "Rational approach for evaluating fire resistance of FRP-strengthened concrete beams", *J. Compos. Constr.*, **20**(6), 04016041.

Hasni, H., Jiao, P., Alavi, A.H., Lajnef, N. and Masri, S.F. (2017), "Structural health monitoring of steel frames using a network of self-powered strain and acceleration sensors: A numerical study", *Automat. Construct.*, **85**, 344-357.

Mazzotti, C., Savoia, M. and Ferracuti, B. (2009), "A new single-shear set-up for stable debonding of FRP-concrete joints", *Constr. Build. Mater.*, **23**(4), 1529-1537.

Soleimani, S., Jiao, P., Rajaei, S. and Forsati, R. (2017), "A new approach for prediction of collapse settlement of sandy gravel soils", *Eng. Comput.*

Teng, J.G., Yuan, H. and Chen, J.F. (2006), "FRP-to-concrete interfaces between two adjacent cracks: Theoretical model for debonding failure", *J. Sol. Struct.*, **43**, 5750-5778.

Tuakta, C. and Buyukozturk, O. (2011), "Deterioration of FRP/concrete bond system under variable moisture conditions

quantified by fracture mechanics", *Compos. B: Eng.*, **42**(2), 145-154.
Ouyang, Z. and Wan, B., (2009), "Nonlinear deterioration model for bond interfacial fracture energy of FRP-concrete joints in moist environments", *J. Compos. Constr.*, **13**(1), 53-63.
Rice, J.R. (1988), "Elastic fracture mechanics concepts for interfacial cracks", *J. Appl. Mech.*, **55**(1), 98-103.
Wang, J. and Qiao, P. (2004), "Interface crack between two shear deformable elastic layers", *J. Mech. Phys. Sol.*, **52**, 891-905.
Wu, Z.S., Yuan, H. and Niu, H. (2002), "Stress transfer and fracture propagation in different kinds of adhesive joints", *J. Eng. Mech.*, **128**(5), 562-573.
Xiao, J., Huang, Y., Yang, J. and Zhang, C. (2012), "Mechanical properties of confined recycled aggregate concrete under axial compression", *Constr. Build. Mater.*, **26**(1), 591-603.
Yuan, H., Teng, J.G., Seracino, R., Wu, Z.S. and Yao, J. (2004), "Full-range behavior of FRP-to-concrete bonded joints", *Eng. Struct.*, **26**(5), 553-565.

CC